# CrystEngComm

Accepted Manuscript






ROYAL SOCIETY OF CHEMISTRY

www.rsc.org/crystengcomm

# Rapid synthesis of photocatalytic $(BiO)_2CO_3$ single-crystal nanosheets via an eco-friendly approach

Fan Dong[a,*], Ji Bian[a], Yanjuan Sun[a], Ting Xiong[a], Wendong Zhang[b]

[a] Chongqing Key Laboratory of Catalysis and Functional Organic Molecules, College of Environmental and Biological Engineering, Chongqing Technology and Business University, Chongqing, 400067, China,

[b] College of Urban Construction and Environmental Engineering, Chongqing University, Chongqing, 400045, China



* To whom correspondence should be addressed. Tel/Fax: + 23-62769785-605, E-mail: dfctbu@126.com (Fan Dong)

**Abstract:** $(BiO)_2CO_3$ single-crystal nanosheets were successfully fabricated via an eco-friendly aqueous process using $CO_2$ and bismuth nitrate as raw materials under mild conditions within 30 min. Compared with previous preparation methods, this facile method avoids treatment at high temperature, use of organic precursors and production of undesirable organic byproducts during synthesis process. The as-prepared samples were characterized by XRD, SEM, TEM, BET-BJH measurement, UV-vis DRS, FT-IR, Time-resolved ns-level PL in detail. It was found that the size and the thickness of $(BiO)_2CO_3$ nanosheets can be influenced by reaction temperature and $CO_2$ concentration. The as-prepared $(BiO)_2CO_3$ nanosheets were applied to photocatalytic removal of NOx under artificial UV–vis and UV light irradiation and showed admirable photocatalytic performance. Significantly, $(BiO)_2CO_3$ nanosheets can be directly fabricated using the $CO_2$ in air without extra separation process, and the as-prepared $(BiO)_2CO_3$ nanosheets exhibited efficient and durable photocatalytic performance for NOx removal. The present work developed a novel method utilizing $CO_2$ to produce functional $(BiO)_2CO_3$ nanosheets with potential applications in environment and energy, which is expected to fabricate other functional metal carbonate.

***Keywords***: $(BiO)_2CO_3$ nanosheets, carbon dioxide, eco-friendly approach, photocatalytic performance, rapid synthesis.

## 1. Introduction

Recently, two-dimensional (2D) nanostructures such as nanoplates and nanosheets are of particular interests due to their intriguing, unusual properties and potential applications in various fields.[1-3] Graphene nanosheet, a typically 2D nanostructure, has been found to exhibit intriguing properties in optical[4] and electronic devices,[5] energy generation and storage,[6] hybrid materials,[7] and sensors,[8] which subsequently stimulates the interest in nanosheets of various materials such as graphitic carbon nitrides(g-$C_3N_4$),[9] transition metal dichalcogenides,[10,11] transition metal oxides,[12] BN[13, 14] and other 2D compounds. These 2D nanomaterials are expected to possess desirable properties comparable or complementary to that of graphene. Consequently, numerous efforts have been devoted to exploring their synthesis and unique morphology or structure dependent properties.

For photocatalytic materials, 2D nanosheets or nanoplates-like materials exhibit intriguing photocatalytic performance due to the enhanced surface areas, good crystallinity, high structured anisotropy, exposed active facets or effective charge transfer and separation. For example, g-$C_3N_4$ nanosheets with large surface areas showed improved photocatalytic activities compared to the bulk g-$C_3N_4$.[15] BiOCl single-crystalline nanosheets with exposed {001} facets exhibited high activity for photodegradation of methyl orange under UV light.[16] In addition, the 2D layered nanojunctions such as $TiO_2$/graphene,[17] $Bi_2S_3$/BiOI[18] also showed enhanced photocatalytic activity towards removal of pollutants mainly because of the effective charge transfer and separation. Obviously, 2D nanostructures play a significant role in

enhancing the photocatalytic activity due to their distinct properties.

Recently, $(BiO)_2CO_3$, a type of Sillén phase material consists of alternative layers of $[Bi_2O_2]^{2+}$ and $CO_3^{2-}$ groups, has drawn considerable attention due to its promising antibacterial performance and photocatalytic activity. Up to now, various $(BiO)_2CO_3$ nanostructures including nanoparticles,[19] nanotubes,[20] nanoplates,[19,21] nanosheets,[22] nanocubes,[23] flower-like microsphere[24], hollow microsphere[25] and other 3D hierarchical nanostructures have been fabricated by different synthetic routes, such as template-assisted synthesis, hydro-/solvothermal routes, reflux method and so on. Among them, $(BiO)_2CO_3$ nanosheets and nanoplates exhibit excellent photocatalytic properties, which have mainly been fabricated by hydro-/solvothermal methods. For example, Zhao et al. hydrothermally synthesized plate-like $(BiO)_2CO_3$ at 180℃ in a span of 24 h.[21] Chen et al. fabricated $(BiO)_2CO_3$ nanoplates by solvotherml method.[19] Likewise, Huang and co-worker obtained $(BiO)_2CO_3$ nanosheets through hydro- and solvo-thermal processes.[22] However, these methods suffer from high temperature and long reaction time. Thus, it is still a big challenge to develop a simple and fast route to prepare 2D $(BiO)_2CO_3$ nanostructures with well defined shapes and good crystallinity.

Our group recently have fabricated various $(BiO)_2CO_3$ nanostructures with highly active photocatalytic performance using a bottom-up aqueous approach.[25-31] Carbonate and bismuth ions were provided simultaneously in the aqueous solution to form $(BiO)_2CO_3$ nanostructures during fabrication. This simple chemical reaction inspires us to design new approach to fabricate functional $(BiO)_2CO_3$ nanostructures using $CO_2$ as raw material based on the fact that $CO_2$ can be simply transformed to

carbonate ions in basic aqueous environment.

In the present work, we developed an eco-friendly aqueous process to fabricate $(BiO)_2CO_3$ nanosheets using $CO_2$ and bismuth nitrate as raw materials under mild conditions. This aqueous chemical approach to functional $(BiO)_2CO_3$ nanosheets features process simplicity, mildness and scalability. The effects of reaction temperature and $CO_2$ concentration on the microstructure and photocatalytic performance were investigated. Going further, $(BiO)_2CO_3$ nanosheets were directly fabricated using air as $CO_2$ feed stock without extra separation process, and the as-prepared $(BiO)_2CO_3$ showed high performance in the removal of NOx under artificial UV–vis light irradiation. The present work could be further extended to fabricate other functional metal carbonates (e.g., $Ag_2CO_3$, $SrCO_3$) in economical and ecological way competitive to current technologies.

## 2. Experimental

### 2.1 Formation of $(BiO)_2CO_3$ nanosheets

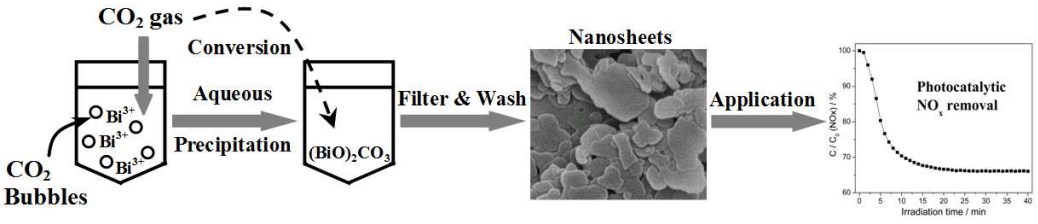


**Fig. 1** Schematic illustration of the experimental procedure for conversion of $CO_2$ gas to $(BiO)_2CO_3$ nanosheets and the photocatalytic application.

All the chemicals used in this study were analytical grade and were used without

95 further purification. Distilled water was used in all experiments. In a typical synthesis,
96 certain amount of $Bi(NO_3)_3 \cdot 5H_2O$ (1.21g) were dissolved in 100 mL of nitric acid
97 solution (0.9 mol/L) and stirred for 50 min. Then, 15 mL of concentrated ammonia
98 solution was added and white precipitate was produced. $CO_2$ gas stream (1.0 L/min)
99 was introduced to the above suspension with stirring and maintained for 30 min. After
100 the gas stream was closed, the resulted precipitate was filtered, washed with water and
101 ethanol for four times and dried at 60 $^oC$ to get the final $(BiO)_2CO_3$ with no further
102 treatment. In order to investigate the effects of reaction temperature and $CO_2$
103 concentration, the reaction temperature and the $CO_2$ concentration were varied. The
104 samples prepared at temperature of 25, 45, 65 and 85 $^oC$ with $CO_2$ concentration of
105 100% were labeled as BOC-T25, BOC-T45, BOC-T65 and BOC-T85, respectively.
106 The samples prepared at $CO_2$ concentration of 0.1, 1, 10 and 100% under reaction
107 temperature of 45 $^oC$ were labeled as BOC-C0.1, BOC-C1, BOC-C10 and BOC-C100,
108 respectively. The experimental procedure for conversion of $CO_2$ gas to $(BiO)_2CO_3$
109 nanosheets and their photocatalytic application was illustrated in Fig. 1.

110 For the sample prepared using $CO_2$ in air as raw material at room temperature, the
111 $CO_2$ gas stream was replaced by pumped air stream at a flow rate of 1.0 L/min for 3 h
112 with other conditions identical. The resulted sample was labeled as BOC-Air.

113 For the hydrothermal synthesis of $(BiO)_2CO_3$, appropriate amounts of bismuth
114 citrate (1.60 g) and sodium carbonate (0.46 g) were mixed with 75 mL of $H_2O$ in a
115 100 mL autoclave Teflon vessel and stirred for 30 min. The resulting aqueous
116 precursor suspension was then hydrothermally treated at 210 $^oC$ for 24 h. The sample

obtained was filtered, washed with water and ethanol three times and dried at 60 $^{o}$C for 12 h to get final $(BiO)_2CO_3$ samples with no further treatment. This sample was labeled as BOC-H.

## 2.2 Characterization

The crystal phase was analyzed by X-ray diffraction with Cu Kα radiation (XRD: model D/max RA, Japan) at a scan rate of 0.01$^{o}$ 2θ/s. FT-IR spectra were recorded on a Nicolet Nexus spectrometer on samples embedded in KBr pellets. A scanning electron microscope (SEM, JEOL model JSM-6490, Japan) was used to characterize the morphology of the samples. The morphology and micostructure were examined by transmission electron microscopy (TEM: JEM-2010, Japan). The UV-vis diffuse reflection spectra were obtained for the dry-pressed disk samples using a Scan UV-vis spectrophotometer (UV-vis DRS: UV-2450, Shimadzu, Japan) equipped with an integrating sphere assembly, using $BaSO_4$ as reflectance sample. The photoluminescence spectra were measured with a fluorescence spectrophotometer (F-7000, Japan) using a Xe lamp as excitation source with optical filters. Nitrogen adsorption-desorption isotherms were obtained on a nitrogen adsorption apparatus (ASAP 2020, USA) with all samples degassed at 50°C for 12 h prior to measurements. Time-resolved photoluminescence (PL) spectroscopy was recorded on FLsp920 Fluorescence spectrometer (Edinburgh Instruments) with excitation at 330 nm.

## 2.3 Evaluation of photocatalytic activity

The photocatalytic activity was investigated by removal of NO at ppb levels in a continuous flow reactor at ambient temperature. The volume of the rectangular reactor, made of stainless steel and covered with Saint-Glass, was 4.5 L (30 cm × 15 cm × 10 cm). A 150 W commercial tungsten halogen lamp was vertically placed outside the reactor. Photocatalyst (0.1 g) was coated onto a dish with a diameter of 12.0 cm. The coated dish was then pretreated at 70 $^{o}$C to remove water in the suspension. Two dishes were placed in the reactor. The NO gas was acquired from a compressed gas cylinder at a concentration of 100 ppm of NO ($N_2$ balance, BOC gas). The initial concentration of NO was diluted to about 600 ppb by the air stream. The desired relative humidity (RH) level of the NO flow was controlled at 50% by passing the zero air streams through a humidification chamber. The gas streams were premixed completely by a gas blender, and the flow rate was controlled at 2.4 L/min by a mass flow controller. After the adsorption-desorption equilibrium was achieved, the lamp was turned on. The concentration of NO was continuously measured by a chemiluminescence NO analyzer (Thermo Environmental Instruments Inc., 42i-TL), which monitors NO, and $NO_2$ with a sampling rate of 1.0 L/min. The removal ratio ($\eta$) of NO was calculated as $\eta$ (%) = (1-$C/C_0$) ×100%, where $C$ and $C_0$ are concentrations of NO in the outlet steam and the feeding stream, respectively. The kinetics of photocatalytic NO removal reaction is a pseudo first order reaction at low NO concentration which can be decried as $\ln(C_0/C) = kt$, where $k$ is the apparent rate constant.

# 3. Results and discussion

## 3.1 Phase structure

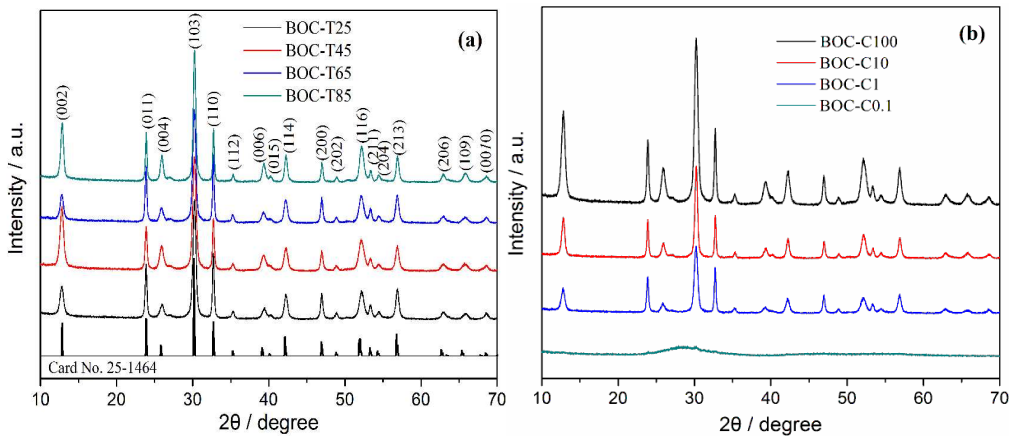


**Fig. 2** XRD patterns of the samples obtained at different temperatures (a) and different $CO_2$ concentrations (b).

Fig. 2a shows the XRD patterns of the samples obtained at different reaction temperatures compared with standard PDF card. The diffraction peaks for each sample can match the orthorhombic $(BiO)_2CO_3$ crystallites (JCPDS file No. 25-1464). No peaks of any other phases or impurities are detected. The reaction temperature has no obvious effect on the phase structure of $(BiO)_2CO_3$. As the reaction temperature increases, the crystallinity of the samples is slightly improved. This fact can be attributed to the high thermal energy at elevated temperatures that may allow $Bi^{3+}$ and $CO_3^{2-}$ ions to overcome the activation energy barrier and to accelerate the nucleation and growth of $(BiO)_2CO_3$ crystallites.[32] Fig. 2b shows the XRD patterns of the samples obtained under different $CO_2$ concentrations. When the $CO_2$ concentration is set 0.1%, the resulting sample is amorphous. When the $CO_2$ concentration increases from 1% to 100%, $(BiO)_2CO_3$ crystallites are produced. Further observation indicates

that the intensity of the diffraction peaks for each sample is strengthened with increased $CO_2$ concentration, which suggests that the crystallinity of the samples is enhanced gradually.

The formation of $(BiO)_2CO_3$ follows the following simple chemical reactions (Eq. 1-4). Considering the yield of $(BiO)_2CO_3$, all the $Bi(NO_3)_3 \cdot 5H_2O$ used were transformed to $(BiO)_2CO_3$ product under the present conditions.

$$NH_3 + H_2O \longrightarrow NH_4^+ + OH^- \quad (1)$$

$$Bi^{3+} + NO_3^- + 2OH^- \longrightarrow BiONO_3\downarrow + H_2O \quad (2)$$

$$CO_2 + 2OH^- \longrightarrow CO_3^{2-} + H_2O \quad (3)$$

$$BiONO_3\downarrow + CO_3^{2-} \longrightarrow (BiO)_2CO_3\downarrow + 2NO_3^- \quad (4)$$

According to the crystal structure of $(BiO)_2CO_3$, the $(Bi_2O_2)^{2+}$ layers and $CO_3^{2-}$ layers are inter-grown with the plane of the $CO_3^{2-}$ group orthogonal to the plane of the $(Bi_2O_2)^{2+}$ layer. The internal layered structure would naturally guide the lower growth rate along certain axis to form two-dimensional nanosheets.[29] These facts indicate that the well-crystallized $(BiO)_2CO_3$ can be produced in a short time using inorganic precursors.

Fig. S1 shows the FT-IR of the samples obtained at different conditions. The samples prepared at reaction temperature between 25 and 85 $^oC$ and with $CO_2$ concentration from 1 to 100% have similar vibration peaks (Fig. S1a and S1b). The "free" $CO_3^{2-}$ ions (point group symmetry $D_{3h}$) exhibit four internal vibrations, including symmetric stretching mode $\nu_1$ (1067 $cm^{-1}$), the corresponding anti-symmetric vibration $\nu_3$ (1468 and 1391 $cm^{-1}$), the out-of-plane bending mode $\nu_2$

(846 and 820 $cm^{-1}$) and the in-plane deformation $\nu_4$ (698 and 670 $cm^{-1}$). The band groups of $\nu_1 + \nu_4$ (1756 and 1730 $cm^{-1}$) can be also observed. The broad peaks at 1500-1600 $cm^{-1}$ and 3400-3600 $cm^{-1}$ can be assigned to the characteristic stretching vibrations of surface hydroxyl groups from absorbed water molecules.[30] Fig. S1b shows that the sample prepared with $CO_2$ concentration of 0.1% has minor amount of $(BiO)_2CO_3$ as the $CO_3^{2-}$ ions supplied by $CO_2$ were not enough to finish the complete transformation.

### 3.2 Morphology

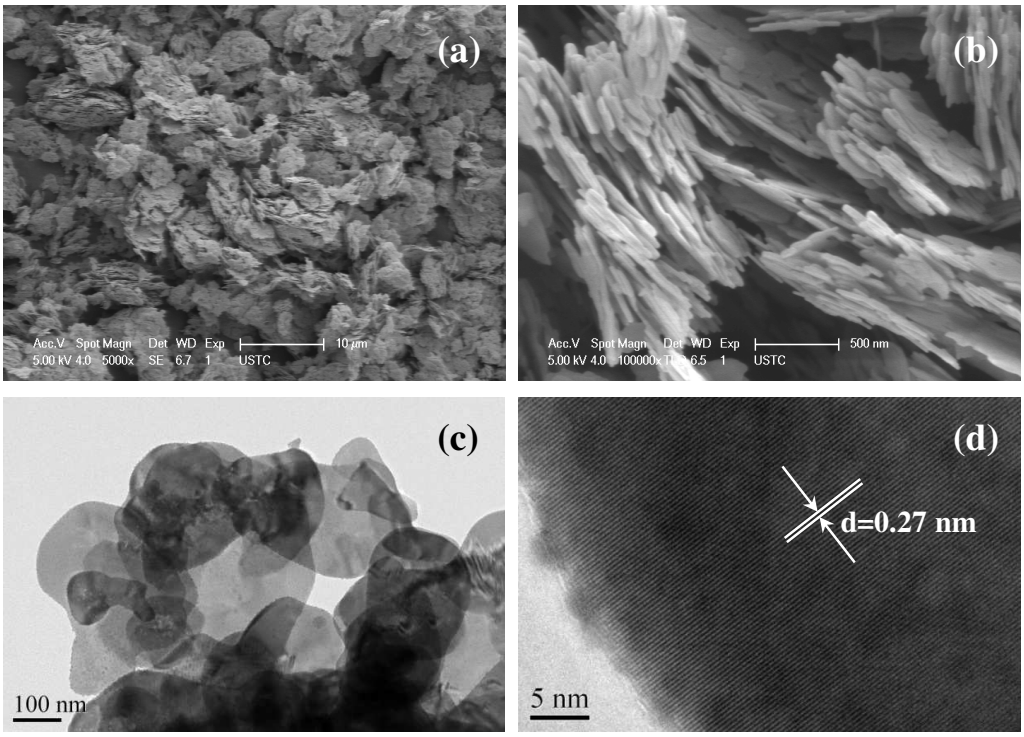


**Fig. 3** SEM (a, b) and TEM (c, d) images of BOC-C1.

The low-magnification SEM image of Fig. 3a reveals that the BOC-C1 sample is composed of a large amount of randomly aggregated nanosheets. The magnified image in Fig. 3b shows that all the nanosheets have an irregular morphology with

thickness of 20-30 nm. TEM image in Fig. 3c shows that the BOC-C1 sample is composed of well-defined nanosheets. The yield of the nanosheets morphology reaches 100%. The lattice spacing *d* value is determined to be 0.27 nm (Fig. 3d), matching with the spacing of the (110) crystal plane of $(BiO)_2CO_3$.

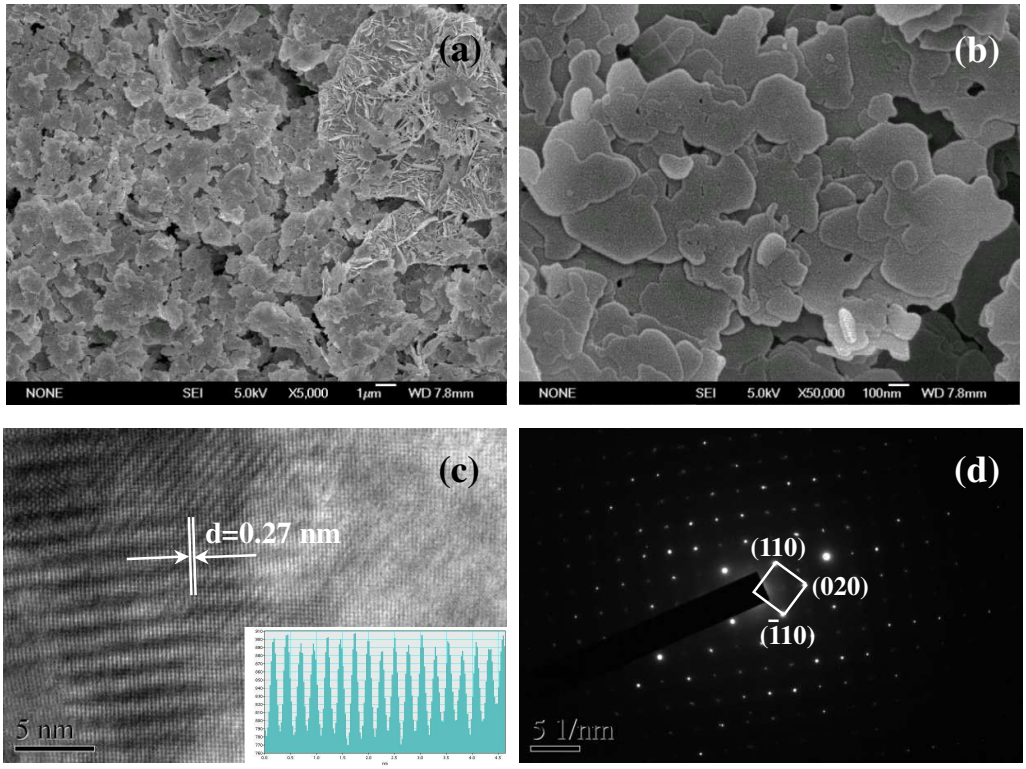


**Fig. 4** SEM (a, b), HRTEM (c) images and SAED (d) of BOC-C10.

When the $CO_2$ concentration is increased to 10%, large amount of nanosheets with relatively large size are produced, as shown in Fig. 4a. These nanosheets are attached together in a layer-by-layer style. Fig. 4b shows that the surface of the nanosheet is smooth and the shape is irregular. The thickness of the nanosheets is increased to 30-40 nm. Fig. 4c shows the HRTEM image of a single nanosheet. The lattice spacing *d* value is determined to be 0.27 nm, matching with the spacing of the (110) crystal plane of $(BiO)_2CO_3$. The SAED pattern (Fig. 4d) with well alignment implies that the

nanosheet is single-crystal. The diffraction spots of the SAED pattern can be indexed as the (110), ($\bar{1}$10) and (020) reflections, suggesting that the exposed wide facet of the nanosheet is (002) plane.

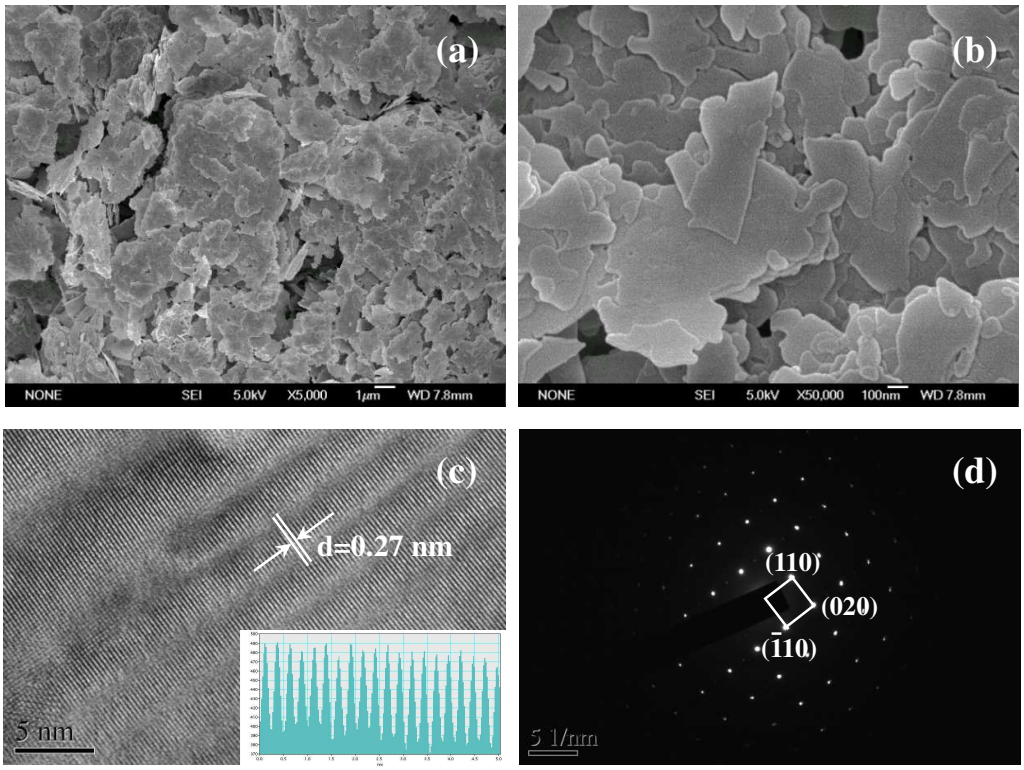


**Fig. 5** SEM (a, b), HRTEM (c) images and SAED (d) of BOC-C100 (BOC-T45).

When the $CO_2$ concentration is increased to 100%, large amount of nanosheets can also be produced as shown in Fig. 5a. It seems that the average size of the nanosheets is further increased (Fig. 5b). The thickness of the nanosheets is further increased to 40-50 nm. The HRTEM image of a single nanosheet shows that the lattice spacing *d* value is 0.27 nm, assigning to the spacing of the (110) crystal plane of $(BiO)_2CO_3$. The SAED pattern (Fig. 5d) is similar to that of BOC-C10. That is, the nanosheet with (002) planes exposed is also single-crystalline. Combing the Fig. 3, 4 and 5, we can find that the size and thickness of the single-crystal nanosheets was increased with the

increased $CO_2$ concentration.

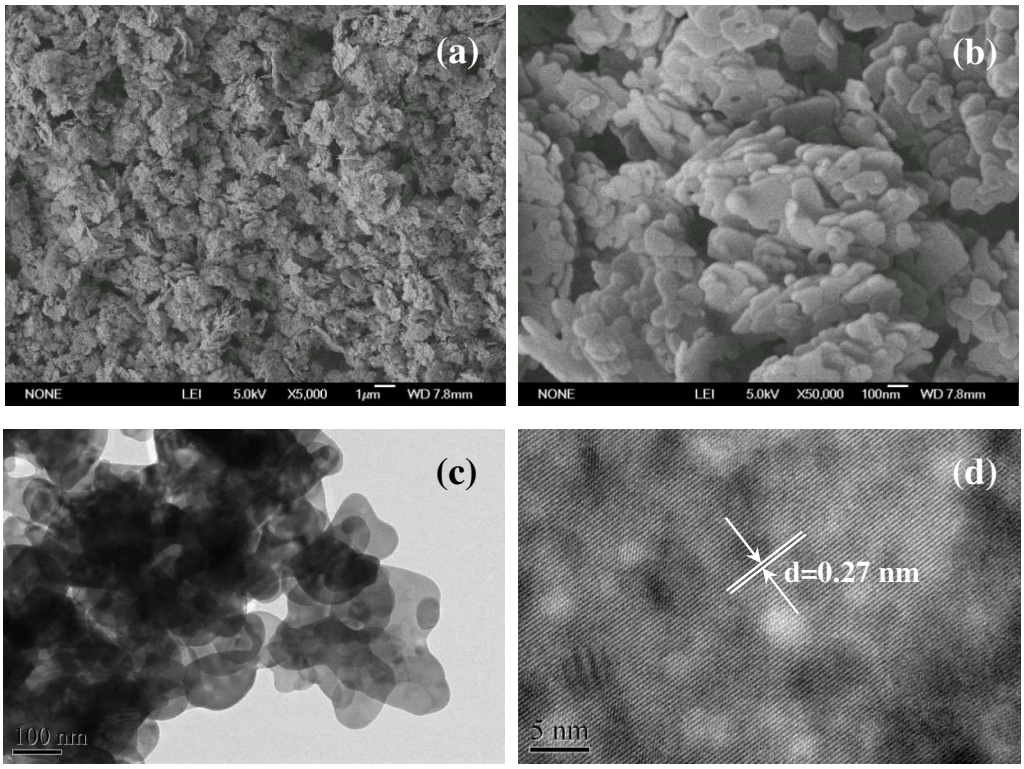


**Fig. 6** SEM (a, b) and TEM (c, d) images of BOC-T25.

At low reaction temperature of 25 °C, the size of the nanosheets is significantly reduced (Fig. 6a and 6b) probably due to slow reaction rate. The TEM image (Fig. 6c) shows that the BOC-T25 sample is also composed of nanosheets. The HRTEM image shows the lattice spacing *d* value of a single nanosheet is 0.27 nm, assigning to the spacing of the (110) crystal plane of $(BiO)_2CO_3$.

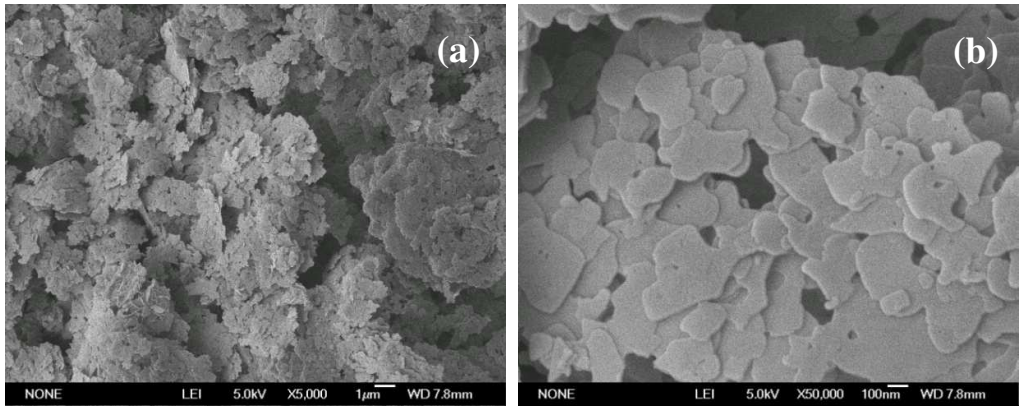

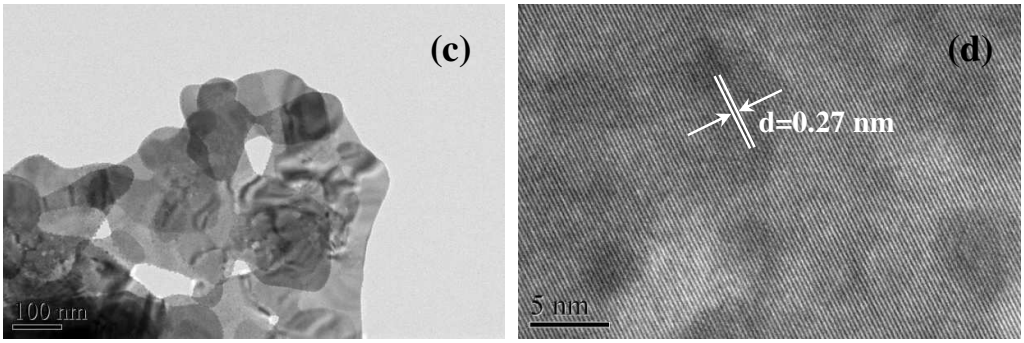


**Fig. 7** SEM (a, b) and TEM (c, d) images of BOC-T65.

When the reaction temperature is raised to 65 °C, the product is transformed to nanosheets with large smooth surface (Fig. 7a and 7b). Note that some pores on the surface of the nanosheets can be observed (Fig. 7b). The TEM image (Fig. 7c) shows thin nanosheets morphology. The lattice spacing *d* value of a single nanosheet is determined to be 0.27 nm with HRTEM image in Fig. 7d, assigning to the spacing of the (110) crystal plane of $(BiO)_2CO_3$.

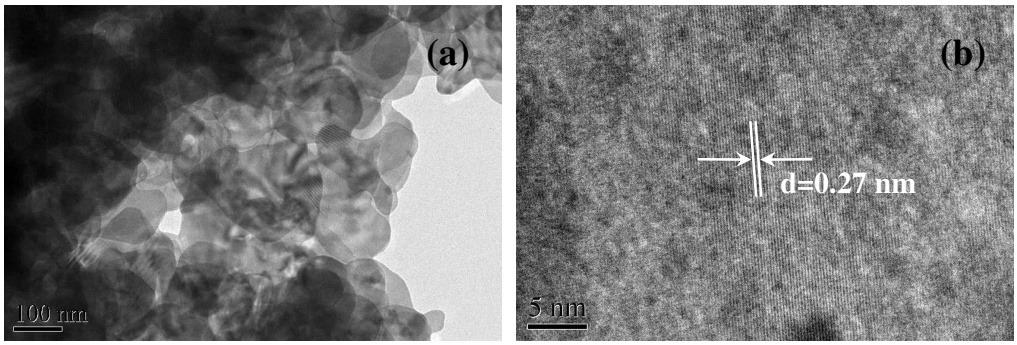


**Fig. 8** TEM (a) and HRTEM (b) images of BOC-T85.

At high reaction temperature of 85 °C, the layered structures are also composed of smooth and thin nanosheets stacked together (Fig. 8a). The HRTEM image (Fig. 8b) reveals clear lattice fringes of single nanosheet with d-spacing of 0.27 nm, which corresponds well with the (110) plane.

### 3.3 Surface areas and pore structure

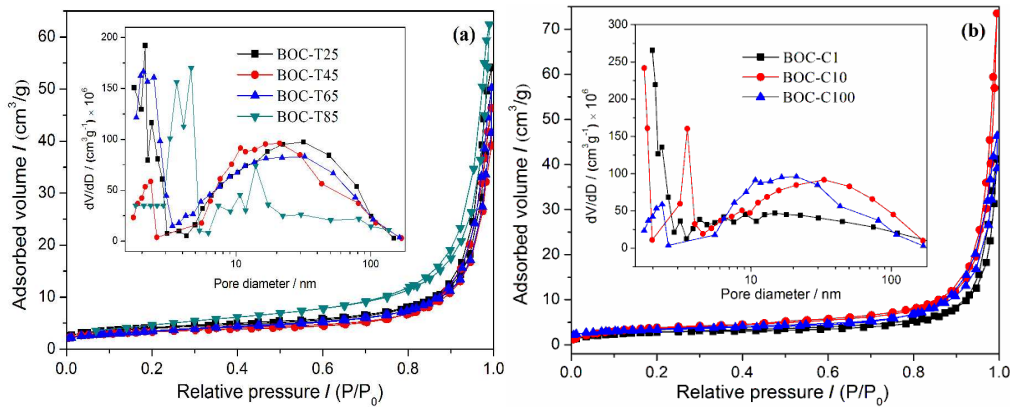


**Fig. 9** BET-BJH of samples obtained at different temperature (a) and different $CO_2$ concentration (b).

Fig. 9 shows the $N_2$ adsorption-desorption isotherms and the corresponding pore size distribution curves of samples obtained at different temperature and different $CO_2$ concentration. All samples exhibit the Type IV isotherms characteristic of mesoporosity.[33] These hysteresis loops with type H3 indicate the formation of slit-like pores due to the aggregations of the sheet-like particles.[33] This is in good agreement with the TEM images (Fig. 3-8). Each sample is composed of aggregated nanosheets. The mesopores can be directly observed from the BJH pore size distribution curves as set in Fig. 9a and 9b. The very small pores can be ascribed to the porosity within the continuous nanosheets. And the large mesopores can be attributed to the pores formed between the aggregated nanosheets. The BET specific surface areas and total pore volume of the samples are shown in Table 1.

**Table 1** The BET surface areas ($S_{BET}$), total pore volume ($V_p$), peak pore volume ($D_P$), NO removal ratio ($\eta$) of $(BiO)_2CO_3$ nanosheets obtained at different temperature

and $CO_2$ concentration.

| Sample | $S_{BET}$ ($m^2$/g) | $V_p$ ($cm^3$/g) | $D_P$ (nm) | $\eta$ (%) |
|---|---|---|---|---|
| BOC-T25 | 15 | 0.084 | 2.1/31.6 | 24.0 |
| BOC-T45 | 12 | 0.071 | 2.3/21.1 | 33.9 |
| BOC-T65 | 13 | 0.078 | 2.0/32.3 | 40.0 |
| BOC-T85 | 17 | 0.096 | 4.6/13.9 | 36.9 |
| BOC-C1 | 11 | 0.063 | 2.3/14.9 | 28.8 |
| BOC-C10 | 14 | 0.11 | 3.5/33.2 | 30.4 |
| BOC-C100 | 12 | 0.071 | 2.3/21.1 | 33.9 |

### 3.4 Optical properties

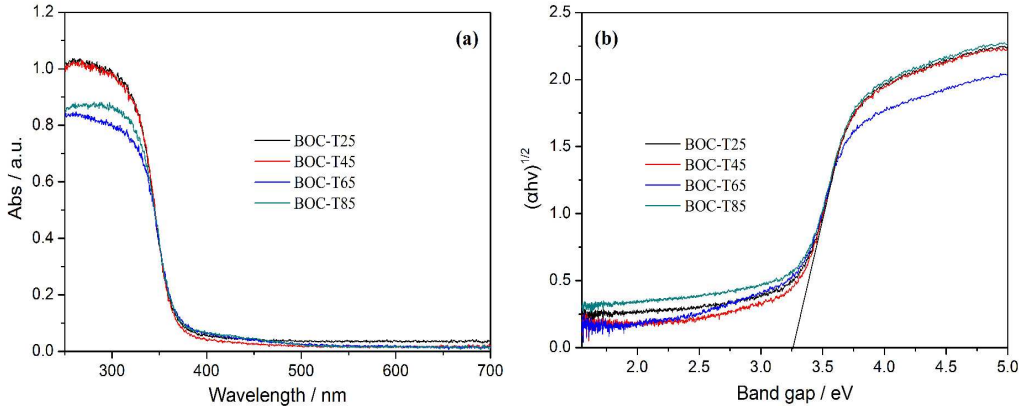

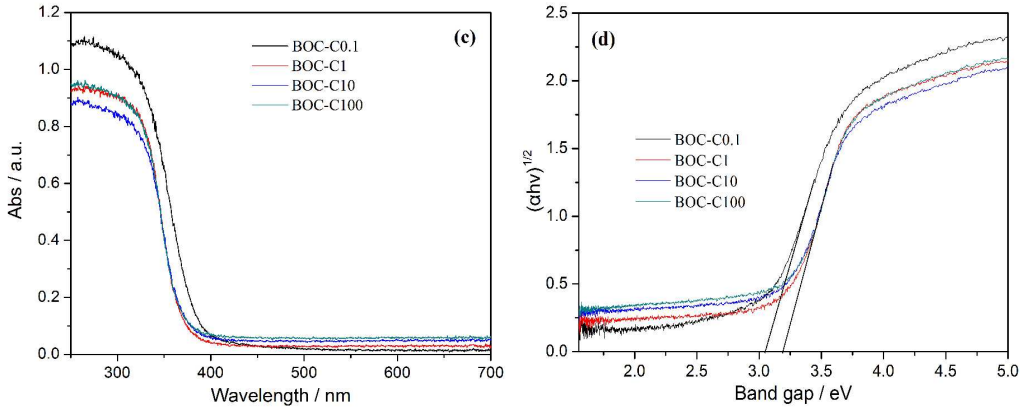


**Fig. 10** UV-vis DRS and plots of $(\alpha h\nu)^{1/2}$ vs. photo energy of samples obtained at different temperature (a, b) and different $CO_2$ concentration (c, d).

Fig. 10 shows the UV-vis DRS spectra and plots of $(\alpha h\nu)^{1/2}$ vs. photo energy for samples obtained at different temperature and different $CO_2$ concentration. The band edge is determined to be 380 and 388 nm for the different temperature and different $CO_2$ concentration samples, respectively. The corresponding band gap energy is calculated to be 3.26 and 3.20 eV, which is consistent with literature values.[34-35] For the amorphous sample prepared with $CO_2$ concentration of 0.1%, the band edge is 407 nm and the band gap energy is 3.05 eV.

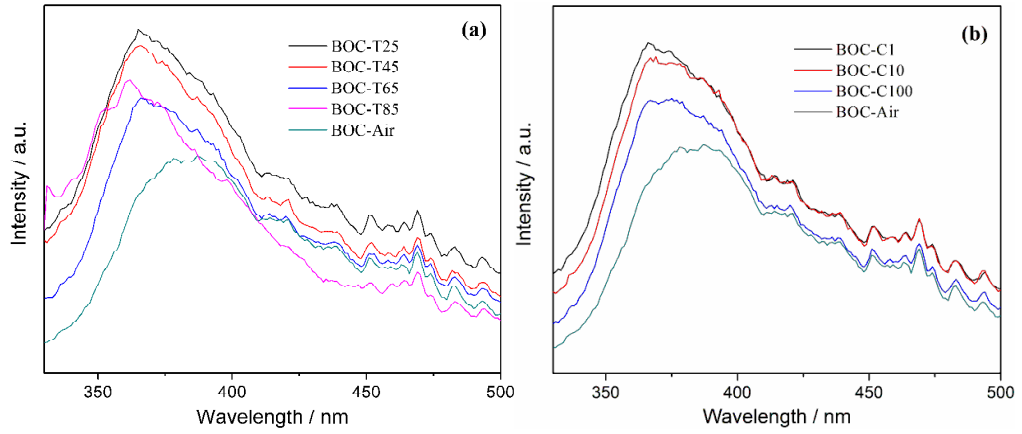


**Fig. 11** Room-temperature PL spectra of samples obtained at different temperature (a) and different $CO_2$ concentration (b), Excitation light source: 310 nm.

Fig. 11 shows the room-temperature PL spectra of samples obtained at different conditions using the excitation light of 310 nm. As PL emission originates from the recombination of excited electrons and holes, the lower PL intensity indicates a higher charge separation rate, which is advantageous for promoting the photocatalytic activity.[36-37] Fig. 11a and 11b shows that the PL intensity of the sample is decreased with increased reaction temperature and $CO_2$ concentration. The change in PL intensity should be probably associated with variation of the structure of the nanosheets. As can be seen from XRD result, the crystallinity of the samples is gradually improved with increased reaction temperature and $CO_2$ concentration. The improved crystallinity is favorable for reduction of structural defects serving as charge recombination center.[38] As a result, PL intensity of the samples is gradually decreased with the improved crystallinity. When the reaction temperature is further raised to 85 $^oC$, the PL intensity is increased probably because the solubility of $CO_2$ in the aqueous solution at high temperature is decreased, which may be not favorable for the formation of $(BiO)_2CO_3$. Note that the $(BiO)_2CO_3$ sample prepared using air as $CO_2$ feed stock has the lowest PL intensity, indicating its potential high photocatalytic activity.

**Table 2.** The kinetics of emission decay parameters of BOC-T25, BOC-T45, BOC-T65 and BOC-T85 samples.

| Samples | Component | Life time (ns) | Relative Percentage (%) | $\chi^2$ |
|---|---|---|---|---|
| BOC-T25 | $\tau_1$ | 0.201 | 100 | 1.083 |
| | $\tau_2$ | - | - | |

| | | | | |
|---|---|---|---|---|
| BOC-T45 | $\tau_1$ | 0.275 | 83.3 | 1.007 |
| | $\tau_2$ | 1.47 | 16.7 | |
| BOC-T65 | $\tau_1$ | 0.444 | 90.9 | 1.035 |
| | $\tau_2$ | 1.945 | 9.1 | |
| BOC-T85 | $\tau_1$ | 0.356 | 100 | 1.003 |
| | $\tau_2$ | - | - | |

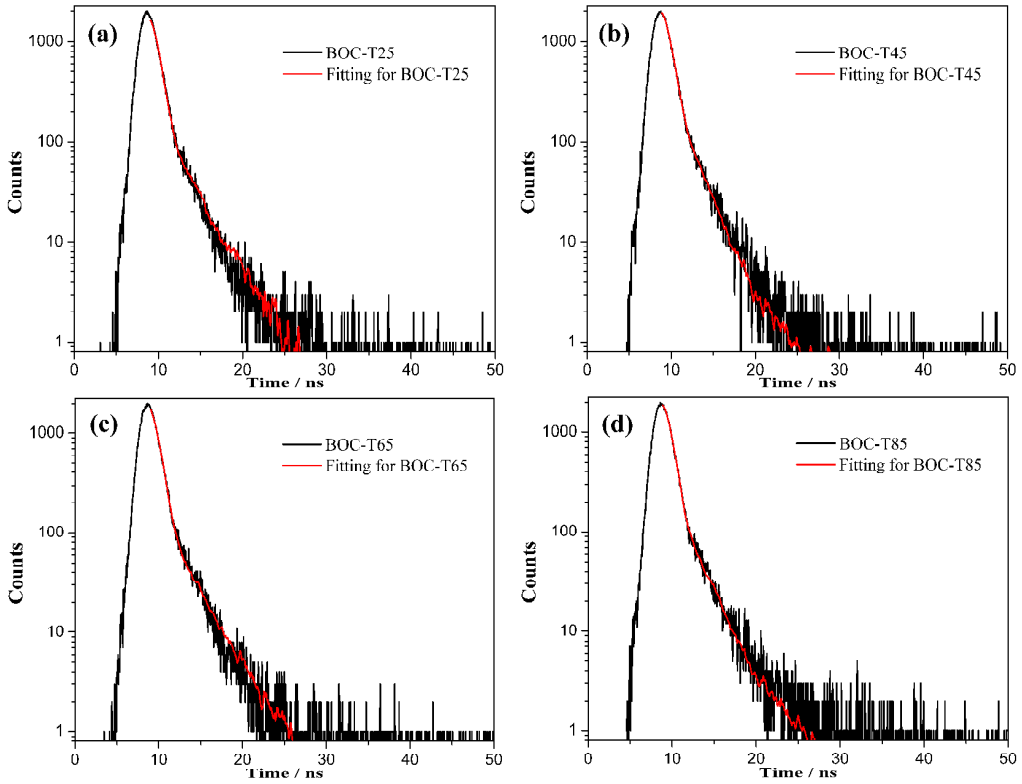


**Fig. 12** Time-resolved ns-level PL spectra at ns-level monitored at 380 nm under the excitation of 330 nm light for BOC-T25 (a), BOC-T45 (b), BOC-T65 (c) and BOC-T85 (d).

In order to understand the carriers transfer kinetics of the samples under irradiation, the time-resolved fluorescence decay spectra at ns-level were recorded as shown in Fig. 12. The radiative lifetime with different ratio can be calculated by fitting the decay spectra as summarized in Table 2. The fluorescence decay kinetics for BOC-T65 is slower than all other samples. The short lifetime ($\tau_1$) of BOC-T25 is

0.201 ns. When the reaction temperature is increased to 65 °C, the short lifetime of BOC-T65 is increased up to 0.444 ns, which is 0.243 ns longer than that of BOC-T25. On the other hand, the long lifetime ($\tau_2$) of charge carriers is increased to 1.945 ns for BOC-T65 and the corresponding percentage of charge carriers with long lifetime is increased simultaneously. The prolonged lifetime of charge carriers is certainly favorable for increasing the number of charge carriers involved in photocatalysis. However, the lifetime of BOC-T85 is decreased. These results imply that the radiative lifetime of all charge carriers are increased by increasing the reaction temperature and then decreased when further increasing the reaction temperature. The variation of lifetime of charge carriers are probably associated with the structural defects induced by the reaction temperature.

### 3.5 Photocatalytic performance for NOx removal

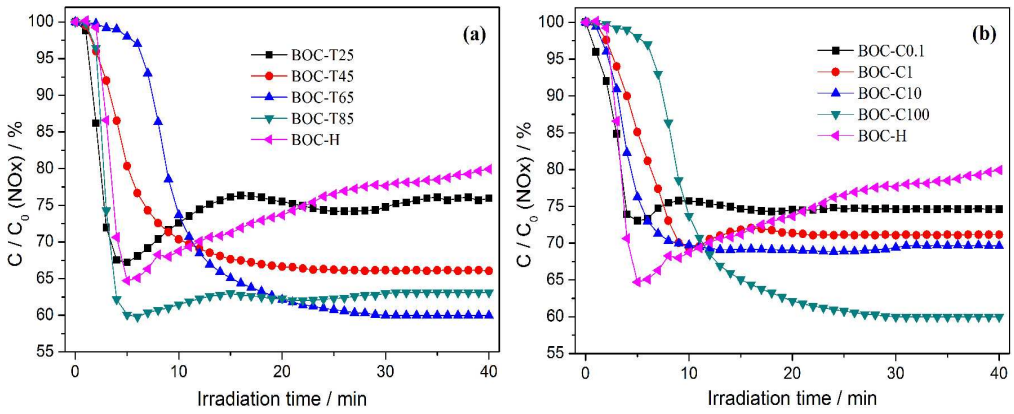


**Fig. 13** The UV–vis photocatalytic removal of NOx over samples obtained at different temperature (a) and different $CO_2$ concentration (b).

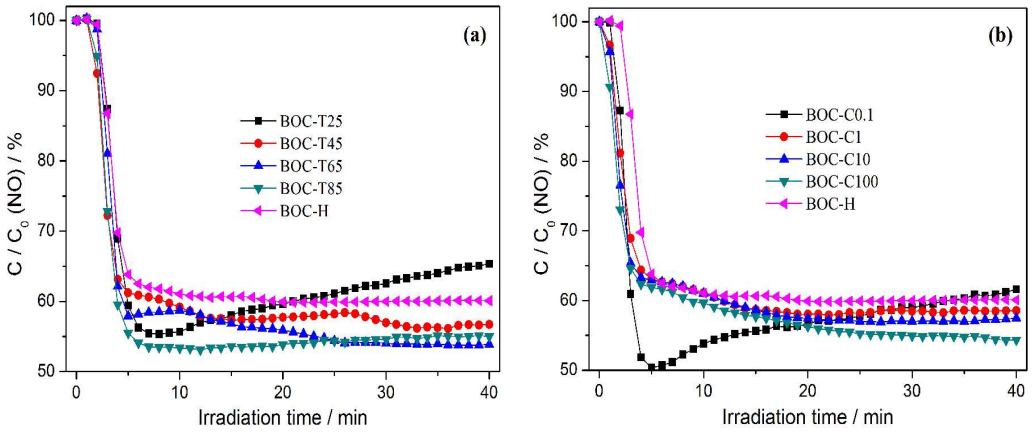


**Fig. 14** The UV photocatalytic removal of NO over samples obtained at different temperature (a) and different $CO_2$ concentration (b).

NOx (NO and $NO_2$), producing from fossil fuels combustion and vehicle exhaust, is a primary air pollutant. It causes adverse implications on atmospheric environment, leading to photochemical smog, acid rain and ozone layer depletion. $(BiO)_2CO_3$ as a semiconductor can be employed as photocatalyst for NOx removal. However, $(BiO)_2CO_3$ exhibits no visible light photocatalytic activity due to its wide band gap energy (Fig. S2). Fig. 13a shows the photocatalytic removal of NOx curves over samples obtained at different temperatures. According to previous reports, the NOx reacted with the photo-generated reactive radicals and produced final $HNO_3$, which involved the following four main reactions in Eqs. (1)-(4).[39-40]

$$NO + 2\ \bullet OH \rightarrow NO_2 + H_2O \quad (1)$$

$$NO_2 + \bullet OH \rightarrow NO_3^- + H^+ \quad (2)$$

$$NO + NO_2 + H_2O \rightarrow 2\ HNO_2 \quad (3)$$

$$NO + \bullet O_2^- \rightarrow NO_3^- \quad (4)$$

As the photocatalytic reaction was going on, the NO concentration in the outlet was decreased gradually due to the conversion of NO to $NO_3^-$. The NO concentration

would reach minima until the photocatalytic reaction reached equilibrium. The slight rising of NO concentration was due to the accumulation of $HNO_3$ product on the catalyst surface. After long term irradiation, the NO concentration in the outlet would reach a steady state. The removal ratio of NOx increased from 24.0 to 40.0% when the reaction temperature increased from 25 to 65 $^oC$, and then reduced to 36.9% when the reaction temperature is further increased to 85 $^oC$. The apparent rate constant ($k$) is 0.0953 $min^{-1}$ for BOC-T25, 0.0445 $min^{-1}$ for BOC-T45, 0.0582 $min^{-1}$ for BOC-T65, and 0.1184 $min^{-1}$ for BOC-T85, respectively. The reaction temperature cannot be further raised because the solubility of $CO_2$ in the aqueous solution would be decreased, which is not favorable for the formation of $(BiO)_2CO_3$.[41] Fig. 13b shows the photocatalytic removal of NOx curves over samples obtained with different $CO_2$ concentration. The removal ratio of NOx increased from 25.4 to 33.9% when the $CO_2$ concentration increased from 0.1 to 100%. The apparent rate constants ($k$) are 0.0654, 0.0343, 0.0575 and 0.0582 $min^{-1}$ for BOC-C0.1, BOC-C1, BOC-C10 and BOC-100, respectively. Fig. 14a and 14b show that all the samples exhibit decent UV photocatalytic removal of NO over samples obtained at different temperature and different $CO_2$ concentration, respectively. The order of the activity of the samples was consistent with the order of the PL intensity and the lifetime of charge carriers. That is, the lower the PL intensity and the longer the carriers lifetime, the higher the photocatalytic activity. Furthermore, $(BiO)_2CO_3$ obtained by the present method demonstrates higher photocatalytic activity than that of $(BiO)_2CO_3$ prepared by hydrothermal method (BOC-H), which demonstrates that our eco-friendly preparation

method is very promising for rapid synthesis of high-performance photocatalysts.

### 3.6 The direct formation of $(BiO)_2CO_3$ nanosheets using $CO_2$ in air and the photocatalytic application

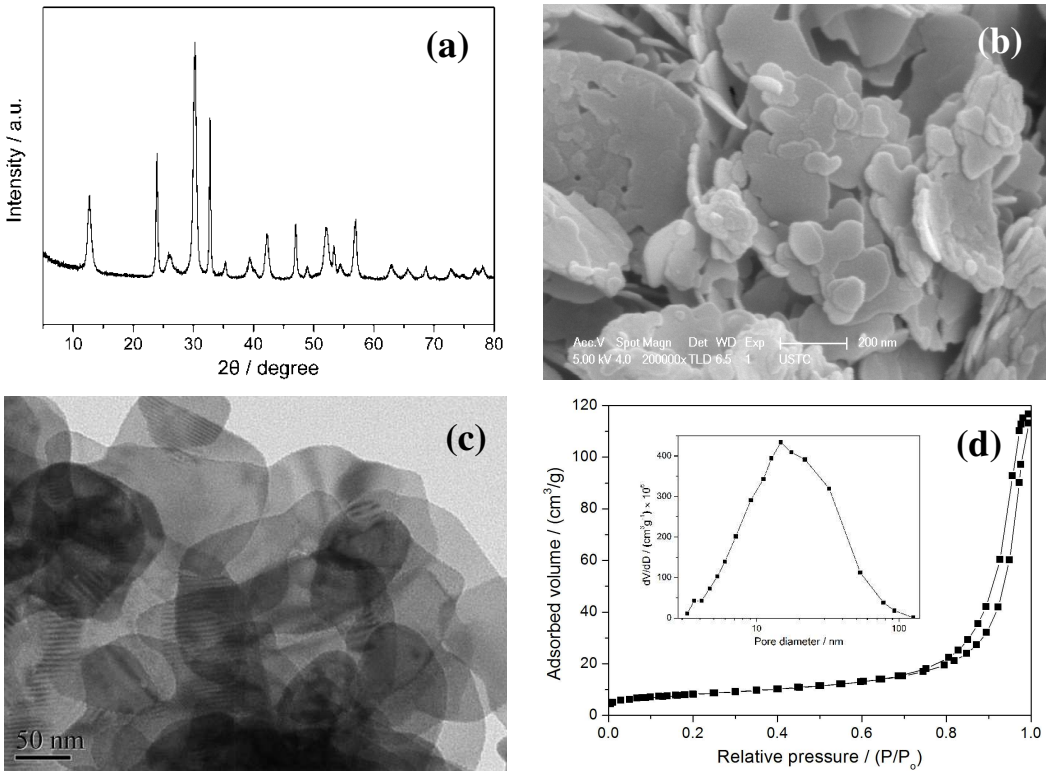


**Fig. 15** XRD pattern (a), SEM image (b), TEM (c) and BET-BJH (d) of $(BiO)_2CO_3$ nanosheets using air as $CO_2$ feeding stock.

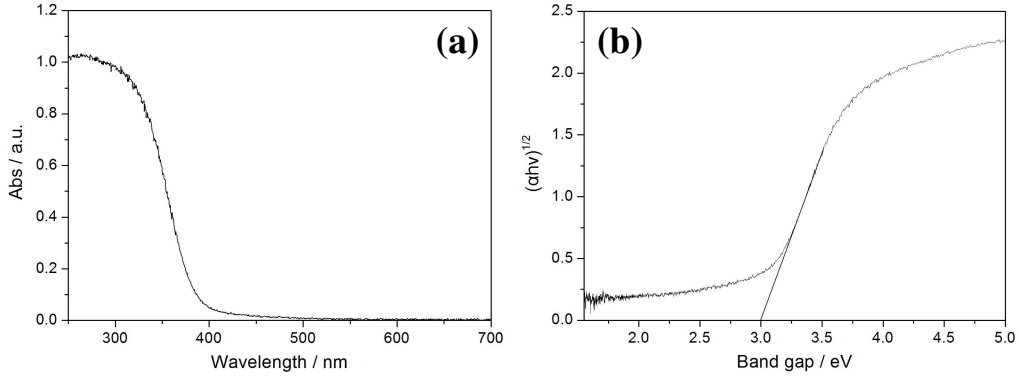


**Fig. 16** UV-vis DRS (a) and plots of $(\alpha h\nu)^{1/2}$ vs. photo energy (b) of $(BiO)_2CO_3$

nanosheets using air as $CO_2$ feeding stock.

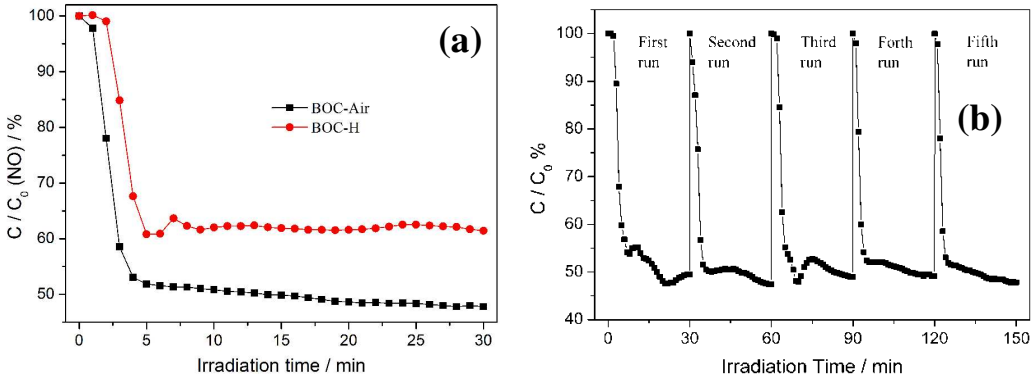


**Fig. 17** Photocatalytic removal (a) and repeated photocatalytic removal (b) of NO of $(BiO)_2CO_3$ nanosheets using air as $CO_2$ feeding stock.

Currently, the $CO_2$ concentration in the air is about 380 ppm. In order to utilize the $CO_2$ in air directly without additional separation, the $CO_2$ gas stream in the fabrication process was replaced by pumped air stream at a flow rate of 1.0 L/min. The air flow was maintained for 3 h and the whole fabrication process was controlled at room temperature. It is amazing to find that the resulted product is orthorhombic $(BiO)_2CO_3$ crystallites in pure phase as shown in Fig. 15a. Fig. 15b and 15c implies that the BOC-Air sample exhibit nanosheets morphology, which is similar to that of the samples in Fig. 3-8. The isotherms of the BOC-Air sample (Fig. 15d) can be classified to type IV, indicating the presence of mesopores. The corresponding pore size distribution of BOC-Air sample (inset in Fig. 15d) further confirms the mesopores (~15 nm). The absorption edge of the BOC-Air sample is determined to be 413 nm (Fig. 16a). The band gap of the BOC-Air ($E_g$) estimated from the intercept of the tangent to the plot of $(\alpha hv)^{1/2}$ vs. photo energy (Fig. 16b) is 3.00 eV. To further test the photocatalytic activity and photochemical stability of the BOC-Air sample for

practical application, multiple reaction tests were carried out. The sample after the first run was used directly without further treatment for the next photocatalytic reaction runs. As shown in Fig. 17a, the activity of BOC-Air sample for removal of NOx is higher than that of other samples. Furthermore, the NOx removal ratios of BOC-Air could be well maintained at 52.2% after five cycles under repeated light irradiation (Fig. 17b). These results clearly demonstrate that $(BiO)_2CO_3$ nanosheets can be directly fabricated using air as $CO_2$ feed stock through an economical and eco-friendly aqueous process, and that the as-prepared $(BiO)_2CO_3$ nanosheets can be applied for efficient photocatalytic air purification. As is known that the photocatalyst could be operated at room temperature and normal pressure, ensuring that the $(BiO)_2CO_3$ photocatalyst has a long lifetime without decomposition or corrosion.

## 4. Conclusion

In summary, a novel eco-friendly approach was developed to fabricate valuable $(BiO)_2CO_3$ single-crystal nanosheets utilize $CO_2$ as raw material for the first time. This facile rapid synthesis method is free of using organic precursors and treating at high temperature. As a functional semiconductor, the as-prepared $(BiO)_2CO_3$ nanosheets can be applied as photoluminescent material for electronics and photocatalyst for pollutant removal. The size and the thickness of $(BiO)_2CO_3$ nanosheets could be controlled by the reaction temperature and $CO_2$ concentration. The as-prepared $(BiO)_2CO_3$ nanosheets exhibited high photocatalytic activity toward removal of NOx in air. Importantly, the $(BiO)_2CO_3$ nanosheets can be directly

fabricated using air as $CO_2$ feed stock, demonstrating its great potential for utilizing $CO_2$ in air without additional separation process, and the $(BiO)_2CO_3$ nanosheets exhibited efficient and durable photocatalytic performance for NOx removal due to the efficient charge separation. The present work provides an economical and convenient approach to synthesize $(BiO)_2CO_3$ nanosheets, which also can be extended to fabricate other functional metal carbonate products.

## Acknowledgements

This research is financially supported by the National Natural Science Foundation of China (51108487), the Natural Science Foundation Project of CQ CSTC (cstc2013jcyjA20018), the Innovative Research Team Development Program in University of Chongqing (KJTD201314, KJTD201020).

**Notes and references**

[1] D. R. Dreyer, R. S. Ruoff and C. W. Bielawski, *Angew. Chem., Int.Ed.,* 2010, **49**, 9336.

[2] M. S. Xu, T. Liang, M. M. Shi and H. Z. Chen, *Chem. Rev.*, 2013, **113(5)**, 3766.

[3] X. F. Song, J. L. Hu and H. B. Zeng, *J. Mater. Chem. C*, 2013, **1**, 2952.

[4] Y. M. Lin, C. Dimitrakopoulos, K. A. Jenkins, D. B. Farmer, H. Y. Chiu, A. Grill and P. Avouris, *Science,* 2010, **327**, 662.

[5] M. Liu, X. B. Yin, E. Ulin-Avila, B. S. Geng, T. Zentgraf, L. Lu, F. Wang, X. Zhang, *Nature,* 2011, **474**, 64.

[6] Y. W. Zhu, S. Murali, M. D. Stoller, K. J. Ganesh, W. W. Cai, P. J. Ferreira, A. Pirkle, R. M. Wallace, K. A. Cychosz, M. Thommes, D. Su, E. A. Stach and R. S. Ruoff, *Science,* 2011, **332**, 1537.

[7] M. F. El-Kady, V. Strong, S. Dubin and R. B. Kaner, *Science,* 2012, **335**, 6074.

[8] M. Deng, X. Yang, M. Silke, W. M. Qiu, M. S. Xu, G. Borghs and H. Z. Chen, *Sensors Actuators B: Chem.* 2011, **158**, 176.

[9] Y. Zheng, J. Liu, J. Liang, M. Jaroniecc and S. Z. Qiao, *Energy Environ. Sci.*, 2012, **5**, 6717.

[10] X. Huang, Z. Y. Zeng and H Zhang, *Chem. Soc. Rev*, 2013, **42**, 1934.

[11] M. Chhowalla, H. S. Shin, G. Eda, L. J. Li, K. P. Loh and H. Zhang, *Nature Chemistry,* 2013, **5**, 263.

[12] M. Osada and T. Sasaki, *Adv. Mater, 2*012, **24,** 210.

[13] M. Sajjad, G. Morell and P. Feng, *ACS Appl. Mater. Interfaces,* 2013, **5**, 5051.

[14] Y. Lin and J. W. Connell, *Nanoscale,* 2012, **4**, 6908.

[15] P. Niu, L. Zhang, G. Liu and H. Cheng, *Adv. Func. Mater.,* 2012, **22**, 4763.

[16] J. Jiang, K. Zhao, X. Y. Xiao and L. Z. Zhang, *J. Am. Chem. Soc.* 2012, **134**, 4473.

[17] D. H. Yoo, T. V. Cuong, V. H. Pham, J. S. Chung, N. T. Khoa, E. J. Kimc and S. H. Hahn, *Current Applied Physics,* 2011, **11**, 805.

[18] J. Cao, B. Y. Xu, H. L. Lin, B. D. Luo and S. F. Chen, *Dalton Trans.*, 2012, **41**, 11482.

[19] R. Chen, G. Cheng, M. H. So, J. L. Wu, Z. Lu, C. M. Che and H. Z. Sun, *Mater. Res. Bull.,* 2010, **45**, 654.

[20] X. F. Cao, L. Zhang, X. T. Chen and Z. L. Xue, *CrystEngComm,* 2011, **13**, 1939.

[21] T. Y. Zhao, J. T. Zai, M. Xu, Q. Zou, Y. Z. Su, K. X. Wang and X. F. Qian, *Cryst. Eng. Comm.*, 2011, **13**, 4010.

[22] Y. Liu, Z. Wang, B. Huang, K. Yang, X. Zhang, X. Qin and Y. Dai, *Appl. Surf. Sci.* 2010, **257**, 172.

[23] J. Tang, G. Cheng, H. Zhou, H. Yang, Z. Lu and R. Chen, *J. Nanosci. Nanotechnol.* 2012, **12**, 4028.

[24] L. Chen, R. Huang, S. F. Yin, S. L. Luo and C. T. Au, *Chem. Eng. J.*, 2012, **193**, 123.

[25] F. Dong, A. M. Zheng, Y.J. Sun, M. Fu, B. Q. Jiang, W. K. Ho, S. C. Lee and Z. B. Wu, *CrystEngComm*, 2012, **14**, 3534.

[26] F. Dong, T. Xiong, Z. W. Zhao, Y. J. Sun and M. Fu, *CrystEngComm*, 2013, **15**,10522.

[27] F. Dong, W. K. Ho, S. C. Lee, Z. B. Wu, M. Fu and S. C. Zou, Y. Huang, *J. Mater. Chem.*, 2011, **21**, 12428.

[28] F. Dong, S. C. Lee, Z.B. Wu, Y. Huang, M. Fu, W. K. Ho, S. C. Zou and B, Wang, *J. Hazard. Mater.,* 2011, **195**, 346.

[29] F. Dong, Y. J. Sun, M. Fu, W. K. Ho, S. C. Lee and Z. B. Wu, *Langmuir*, 2012, **28**, 766.

[30] F. Dong, Y. J. Sun, W. K. Ho and Z. B. Wu, *Dalton Trans.*, 2012, **41**, 8270.

[31] F. Dong, H. T. Liu, W. K. Ho, M. Fu and Z. B. Wu, *Chem. Eng. J*, 2013, **214**, 198.

[32] S. Kim, J. W. Ko and C. B. Park, *J. Mater. Chem.*, 2011, **21**, 11070.

[33] K. S. W. Sing, D. H. Everett, R. A. W. Haul, L. Moscou, R. A. Pierotti, J. Rouquerol and T. Siemieniewska, *Pure Appl. Chem.*, 1985, **57**, 603.

[34] Y. Zheng, F. Duan, M. Q. Chen and Y. Xie, *J. Mol. Catal. A-Chem.*, 2010, **317**, 34.

[35] H. F. Cheng, B. B. Huang, K. S. Yang, Z. Y. Wang, X. Y. Qin, X. Y. Zhang and Y. Dai, *ChemPhysChem*, 2010, **11**, 2167.

[36] Y. Cong, J.L. Zhang F. Chen, M. Anpo and D. N. He, *J. Phys. Chem. C*, 2007, **111**, 10618.

[37] F. Dong, Y. J. Sun and M. Fu, *Inter. J. Photoenergy*, 2012, **2012**, Article ID 569716.

[38] J. G. Yu, L. Zhang, B. Cheng and Y. Su, *J. Phys. Chem. C*, 2007, **111**, 10582.

[39] Z. H. Ai, W. K. Ho, S. C. Lee and L. Z. Zhang, *Environ. Sci. Technol.*, 2009, **43**, 4143.

[40] G. S. Li, D. Q. Zhang, J. C. Yu and M. K. H. Leung, *Environ. Sci. Technol.*, 2010, **44**, 4276.

[41] S. Mignardi, C. D. Vito, V. Ferrini and R. F. Martin, *J. Hazard. Mater.*, 2011, **191**, 49.

# Graphic Abstract

$(BiO)_2CO_3$ single-crystal nanosheets with efficient and durable photocatalytic performance were fabricated using $CO_2$ as feed stock within a short time of 30 min.